INFERENCE OF HEATING PROPERTIES FROM "HOT" NON-FLARING PLASMAS IN ACTIVE REGION CORES I. SINGLE NANOFLARES

W. T. Barnes
Department of Physics & Astronomy, Rice University, Houston, TX 77251-1892

P. J. Cargill
Space and Atmospheric Physics, The Blackett Laboratory, Imperial College, London SW7 2BW and
School of Mathematics and Statistics, University of St. Andrews, St. Andrews, Scotland KY16 9SS

and

S. J. Bradshaw
Department of Physics & Astronomy, Rice University, Houston, TX 77251-1892
Draft version January 14, 2016

ABSTRACT

Abstract will go here.

1. INTRODUCTION

Observations of the magnetically closed solar corona from the *Hinode* (Kosugi et al. 2007) and Solar Dynamics Observatory (SDO) (Pesnell et al. 2012) spacecraft have led, for the first time, to quantitative studies of the distribution of coronal plasma as a function of temperature, and preliminary deductions about the heating process (see papers in De Moortel & Browning 2015). The key to this has been the ability to make measurements of the corona over a wide range of temperatures from the EUV Imaging Spectrometer (EIS) (Culhane et al. 2007) and X-Ray Telescope (XRT) (Golub et al. 2007) instruments on *Hinode*, and the Atmospheric Imaging Assembly (AIA) (Lemen et al. 2012) on SDO. Underpinning this work is the concept of nanoflare heating of the corona. Nanoflares (e.g. Parker 1988) are small bursts of energy release, though, despite the implication in their name, the magnitude and duration are unknown. While commonly attributed to small-scale magnetic reconnection, nanoflares can occur in other heating scenarios (e.g. Ofman et al. 1998).

One example of this approach has been studies of active region core loops (Warren et al. 2011, 2012; Winebarger et al. 2011; Tripathi et al. 2011; Schmelz & Pathak 2012; Bradshaw et al. 2012; Reep et al. 2013; Del Zanna et al. 2015). These are the brightest structures in ARs, spanning the magnetic polarity line, and are observed over a wide range of temperatures. An important result has been the determination of the emission measure distribution as a function of temperature ($EM(T) \sim n^2dh$) along a line of sight. These workers showed that the emission measure peaked at $T = T_m = 10^{6.5}$ – $10^{6.6}$ K with $EM(T_m)$ of order 10^{27} – 10^{28} cm^{-5}. Below T_m a relation of the form $EM \propto T^a$ was found, with $2 < a < 5$. This distribution can be understood by a combination of radiative cooling of the corona to space and an enthalpy flux to the TR (e.g. Bradshaw & Cargill 2010a,b) and is a significant result for nanoflare heating. Defining low and high frequency (LF and HF) nanoflares by the ratio of the average time between nanoflares on a magnetic strand

will.t.barnes@rice.edu

or sub-loop ($\langle T_N \rangle$) to the plasma cooling time from the peak emission measure (τ_{cool}), LF (HF) nanoflares have $\langle T_N \rangle > (<)\tau_{cool}$ respectively. LF nanoflares have $a \sim 2$ - 3 so do not account for many of the observations. In fact, Cargill (2014) argued that these results implied a heating mechanism with $\langle T_N \rangle$ of order 1000 - 2000 s between nanoflares, with the value of T_N associated with each nanoflare being proportional to its energy. Such intermediate frequency (IF) nanoflares have different energy build-up requirements from the commonly assumed LF scenario (Cargill 2014).

A second outcome of AR studies is the detection of a "hot" non-flaring coronal component characterised by plasma with $T > T_m$, a long-predicted consequence of nanoflare heating (Cargill 1994, 1995). This has been identified from *Hinode* and SDO data (Reale et al. 2009; Schmelz et al. 2009; Testa & Reale 2012), and retrospectively from data obtained by the X-Ray Polychromer (XRP) instrument flown on the Solar Maximum Mission (Del Zanna & Mason 2014). While characterising this emission is difficult (e.g. Testa et al. 2011; Winebarger et al. 2012), a similar scaling, $EM \propto T^{-b}$ has been claimed (e.g. Warren et al. 2012), with b of order 7 – 10, though Del Zanna & Mason find larger values. Warren et al. quote typical errors of $\pm$ 2.5 - 3 on these values due to the very limited data available above T_m and Winebarger et al. have noted that the paucity of data from *Hinode* at these temperatures could be missing significant quantities of plasma with $T > T_m$.

In an effort to diminish uncertainty in this high temperature "blind spot" in $EM(T)$, Petralia et al. (2014) analyzed an active region core by supplementing *Hinode*/EIS spectral observations with broadband SDO/AIA and *Hinode*/XRT measurements. By using concurrent observations from the 94 Å channel of AIA and the Ti_poly filter of XRT, the authors showed that the $EM(T)$ peaked near $\log T = 6.6$ and had a weak, hot component. Additionally, Miceli et al. (2012), using the SphinX instrument (Sylwester et al. 2008; Gburek et al. 2011), analyzed full-disk x-ray spectra integrated over 17 days, during which time two prominent active regions were present. These authors found that a two-

temperature model was needed to fit the resulting spectrum, resulting in a strong 3 MK component and a much weaker 7 MK component.

More recent data has come from rocket flights. The Focusing Optics X-ray Solar Imager (FOXSI) (Krucker et al. 2011) first flew in November 2012 and observed an AR. A joint study with the *Hinode* EIS and XRT instruments by Ishikawa et al. (2014) suggested that while hot plasma existed up to 10 MK, the *Hinode* instruments over-estimated the amount of plasma there. A rocket flight reported by Brosius et al. (2014) identified emission in an Fe XIX line with peak formation temperature of $10^{6.95}$ K and reported an emission measure that was 0.59 times the emission formed at $10^{6.2}$ K. More recently, a pair of rocket flights gave observations from the Amptek X123-SDD soft X-ray spectrometer (Caspi et al. 2015). This provided comprehensive coverage of the 3 - 60 Å wavelength range. Caspi et al. demonstrated that the emission in this range could be fit by an emission measure with a power-law distribution slope of roughly $b = 6$.

Several other workers have combined model results with observations in an effort to better elucidate nanoflare signatures. Using a hydrodynamic loop model, Reale et al. (2011) showed that emission from impulsively heated subarcsecond strands is finely structured and that this predicted structure can also be found in AR core emission as observed by the 94 Å channel of AIA. Most recently, Tajfirouze et al. (2016), using a 0D hydrodynamic model, explored a large parameter space in event energy distribution, pulse duration, and number of loops. Using a probabilistic neural network, the authors compared their many forward-modeled light curves to 94 Å AIA observations of a "hot" AR core; they found that the observed light curves were most consistent with a pulse duration of 50 s and a shallow event energy distribution, suggestive of nanoflare heating.

While the distributions of temperature and density above T_m are likely to be determined by nanoflare heating and conductive cooling, there are several complications arising from the low density and high temperature present there. These are (i) the breakdown of the usual Spitzer description of thermal conduction which leads to slower conductive cooling, (ii) recognition that in cases of heating in a weakly collisional or collisionless plasma, electrons and ions need not have the same temperature since when one is heated preferentially the time for the temperature to equilibrate is longer than the electron conductive cooling time, and (iii) a lack of ionization equilibrium that can underestimate the quantity of the plasma with a given electron temperature.

Thus the aim of the present and following paper, Barnes et al. (2016, in preparation) (Paper II, hereafter), is to investigate this high temperature regime with the aim of obtaining information that can be of use in the interpretation of present and future observations. In this paper we focus on single-nanoflare simulations and build up an understanding of the role of the different pieces of physics. Paper II addresses the properties of nanoflare trains. Given the limitations of present observations, the results of both papers are in part predictive for a future generation of instruments. Section 2 addresses our methodology, including simple outlines of the physics expected from conductive cooling, the preferred heating of different species, and ionization non-equilibrium. Section 3 shows results for our single- and two-fluid models, and Section 4 provides discussion of the main points of our results.

2. SUMMARY OF RELEVANT PHYSICS

We begin by assuming that in response to a nanoflare, a coronal loop (or sub-loop) cools by the one-dimensional evolution of a single-fluid plasma ($T_e = T_i$) along a magnetic field line. We deal with the case of electron-ion non-equilibrium in Subsection 2.2. The energy equation is,

$$\frac{\partial E}{\partial t} = -\frac{\partial}{\partial s}[v(E+P)] - \frac{\partial F_c}{\partial s} + Q - n^2\Lambda(T), \quad (1)$$

where v is the velocity, $E = p/(\gamma - 1) + \rho v^2/2$, $F_c = -\kappa_0 T^{5/2}\partial T/\partial s$ is the heat flux, Q is a heating function that includes both steady and time-dependent components, $\Lambda(T) = \chi T^\alpha$ is the radiative loss function in an optically thin plasma (e.g. Klimchuk et al. 2008) and s is a spatial coordinate along the magnetic field. These equations are closed by an equation of state $p = 2nk_BT$. For a given initial state and Q, the plasma evolution can then be followed.

Assuming subsonic flows, Equation 1 and the equation of mass conservation are solved for nanoflare energy input with our zero-dimensional hydrodynamic single fluid EBTEL model (see Klimchuk et al. 2008; Cargill et al. 2012a,b, 2015, for derivations). EBTEL treats the corona and transition region (TR) as separate regions, matched at the top of the TR by continuity of conductive and enthalpy fluxes. EBTEL produces spatially-averaged, time-dependent quantities (e.g. $\bar{T}(t)$, $\bar{n}(t)$) in the corona and can also compute quantities at the loop apex and the corona/TR boundary. The single-fluid EBTEL equations are,

$$\frac{1}{\gamma - 1}\frac{d\bar{p}}{dt} = \bar{Q} - \frac{1}{L}(\mathcal{R}_C + \mathcal{R}_{TR}), \quad (2)$$

$$\frac{\gamma}{\gamma - 1}(pv) + F_{c,0} + \mathcal{R}_{TR} = 0, \quad (3)$$

$$\frac{d\bar{n}}{dt} = -\frac{\gamma - 1}{2k_BT_0L\gamma}(F_{c,0} + \mathcal{R}_{TR}). \quad (4)$$

Here an overbar denotes a coronal average, $F_{c,0} = -(2/7)\kappa_0 T_a^{7/2}/L$ is the heat flux at the top of the TR (see also Subsection 2.1), $\mathcal{R}_C = \bar{n}^2\Lambda(\bar{T})L$, the integrated coronal radiation, $\mathcal{R}_{TR}$ is the integrated TR radiation, and L is the loop half-length. The subscript "0" denotes a quantity at the top of the TR and "a" denotes a quantity at the loop apex. Solving this set of equations requires the specification of three (semi-)constants that are defined by $c_1 = \mathcal{R}_{TR}/\mathcal{R}_C$, $c_2 = \bar{T}/T_a$ and $c_3 = T_0/T_a$. c_2 and c_3 can be taken as constant, with values of 0.9 and 0.6 respectively. c_1 is, in the absence of gravity, 2 for equilibrium, static loops and 0.6 during radiative cooling. Cargill et al. (2012a) discuss the full implementation of $c_1 = c_1(T_a, L)$, and how it can model stratification due to solar gravity. Equation 2 is a statement of energy conservation in the combined corona and TR. Equation 3 is the TR energy equation: if the heat flux into the TR

is greater (smaller) than its ability to radiate then there is an enthalpy flux into (from) the corona. Equation 4 combines the Equation 3 with that of mass conservation.

2.1. *Heat Flux Limiters*

It is well known that thermal conduction deviates from the familiar Spitzer-Härm formula (Spitzer & Härm 1953) at high temperatures (e.g. Ljepojevic & MacNeice 1989). There is a firm upper limit on the heat flux: the free-streaming limit, $F_s = (1/2)fnk_BTV_e$, where V_e is the electron thermal speed and f, a dimensionless constant, is determined from a combination of lab experiments, theory and numerical models. We choose $f = 1/6$ as a typical value. The free-streaming flux is included in EBTEL by a simple modification (Klimchuk et al. 2008),

$$F_{c,0} = \frac{F_c F_s}{\sqrt{F_c^2 + F_s^2}}, \qquad (5)$$

where F_c is the Spitzer-Härm heat flux. Smaller values of f limit the heat flux to a greater degree. The main aspect of inclusion of a free-streaming limit is to slow down conductive cooling. We do not consider here other conduction models (e.g. the non-local model discussed in the coronal context by Karpen & DeVore 1987; Ciaravella et al. 1991; West et al. 2008) since they lead to similar generic results.

2.2. *Two-fluid Modeling*

Additionally, nanoflare heating can also induce electron-ion non-equilibrium if the heating timescale is shorter than the electron-ion equilibration timescale. Interactions between electrons and ions in a fully-ionized hydrogen plasma like the solar corona are governed by binary Coulomb collisions. Thus, the equilbration timescale is $\tau_{ei} = 1/\nu_{ei}$, where ν_{ei} is the collision frequency and is given by

$$\nu_{ei} = \frac{16\sqrt{\pi}}{3}\frac{e^4}{m_e m_i}\left(\frac{2k_B T_e}{m_e}\right)^{-3/2} n \ln\Lambda, \qquad (6)$$

where T_e is the electron temperature, m_e, m_i are the electron and ion masses respectively and $\ln\Lambda$ is the Coulomb logarithm (see Eq. 2.5e and Section 3 of Braginskii 1965). For $n \sim 10^9$ cm^{-3} and $T_e \sim 10^7$ K, parameters typical of nanoflare heating, $\tau_{ei} \approx 800$ s. Thus, any heating that occurs on a timescale less than 800 s, such as a nanoflare with a duration of $\tau_H \leq 100$ s, will result in electron-ion non-equilibrium. While it is true that chromospheric evaporation will act to increase n and thus decrease ν_{ei}, we argue that during the early heating phase, $\tau_{ei} \gg \tau_H$, with 800 s being an upper bound on τ_{ei}.

While it is often assumed that the electrons are the recipients of the prescribed heating function, ion heating in the solar corona should not be discounted since the exact mechanism behind coronal heating is still unknown. For example, ions may be heated via ion-cyclotron wave resonances (Markovskii & Hollweg 2004) or reconnection (Ono et al. 1996; Drake & Swisdak 2014). To address this possibility and include effects due to electron-ion non-equilibrium, we have applied the EBTEL analysis outlined in Klimchuk et al. (2008) to the two-fluid hydrodynamic equations in the form given in the appendix of Bradshaw & Cargill (2013). Such an approach allows us to efficiently model a two-component impulsively-heated coronal plasma.

These expressions, which we will refer to as the two-fluid EBTEL equations, are

$$\frac{d}{dt}\bar{p}_e = \frac{\gamma - 1}{L}[\psi_{TR} - (\mathcal{R}_{TR} + \mathcal{R}_C)] +$$
$$k_B\bar{n}\nu_{ei}(\bar{T}_i - \bar{T}_e) + (\gamma - 1)\bar{Q}_e, \qquad (7)$$

$$\frac{d}{dt}\bar{p}_i = -\frac{\gamma - 1}{L}\psi_{TR} + k_B\bar{n}\nu_{ei}(\bar{T}_e - \bar{T}_i) +$$
$$(\gamma - 1)\bar{Q}_i, \qquad (8)$$

$$\frac{d}{dt}\bar{n} = \frac{c_2(\gamma - 1)}{c_3\gamma Lk_B\bar{T}_e}(\psi_{TR} - F_{ce,0} - \mathcal{R}_{TR}). \qquad (9)$$

This set of equations is closed by the equations of state $p_e = k_B n T_e$ and $p_i = k_B n T_i$. A full derivation of these expressions and the approximations made are given in Appendix A. While the notation above is largely self-evident, we draw attention to the additional term ψ_{TR} which originates in the need to maintain charge and current neutrality and is defined in Equation A23.

2.3. *Ionization Non-equilibrium*

Ionization non-equilibrium has long been known to be an issue in the interpretation of data from the impulsive phase of flares, and more recently it has been discussed in the context of nanoflares (Bradshaw & Cargill 2006; Reale & Orlando 2008). The main issue is that when a tenuous plasma is heated rapidly, it takes a certain time to reach ionization equilibrium so that the ionization states present do not reflect the actual (electron) temperature, assuming that the heating occurs mainly to electrons (see Subsection 2.2 and Subsection 3.3) rather than the heavier ions such as Fe that contribute to the observed radiation. If the heating is sustained, then eventually ionization equilibrium will be reached, and this may occur in moderate to large flares. However, for nanoflares that may last for anywhere between a few seconds and a few minutes, a different scenario arises in which on termination of heating, rapid conductive cooling arises, so that the high ionisation states may never be attained.

Reale & Orlando (2008) and Bradshaw (2009) have both addressed this point using slightly different approaches, but with similar conclusions, namely that short nanoflares in a low-density plasma are unlikely to be detectable. We now develop this work further to assess how the results in Section 3 are changed. We follow these authors and calculate an "effective temperature" (T_{eff}) as a proxy for the deviation from ionization equilibrium. This involves taking a time-series of T and n (e.g. from EBTEL) and using the numerical scheme outlined in Bradshaw (2009) to calculate the fractional ionization of as many states of various elements as needed, and in turn this calculates T_{eff}, a temperature that would be measured based on the actual ionization states. We primarily consider Fe between Fe IX and Fe XXVII, though Ca has also been calculated as a check on these results.

The feature that will prove of great relevance in our results is that despite the different nanoflare durations, T_{eff} does not exceed 10 MK. There is also an "overshot" of T_{eff} when it reaches its maximum value: this is

saying that collisions are still not strong enough for the adjustment of the ionization state to be instantaneous.

3. RESULTS

We now show a series of nanoflare simulations with our zero-dimensional single-fluid hydrodynamic EBTEL model and our modified two-fluid EBTEL model, first for single nanoflares and then in Paper II for nanoflare trains of varying frequency.

In the EBTEL approach, the emission measure for the entire coronal part of the loop is calculated using the familiar expression EM = $n^2(2L)$, where L is the loop half-length. We consider a temperature range of $4.0 \leq \log T \leq 8.5$ with bin sizes of $\Delta \log T = 0.01$. At each iteration i, the coronal temperature range $[T_0, T_a]$ is calculated from $\bar{T}$ ($\bar{T}_e$ for the two-fluid model). For each bin that falls within $[T_0, T_a]$, $\bar{n}_i^2(2L)$ is added to that bin, where $\bar{n}_i$ is the spatially-averaged number density at iteration i. The emission measure in each bin is then averaged over the entire simulation period. When measured observationally, EM(T) is a line-of-sight quantity. Assuming an aspect ratio (i.e. ratio of loop length to loop width) of 10, we apply a correction factor $1/10$ to all calculated EM curves. We do not attempt to apply an advanced forward modeling treatment here and instead reserve such an approach for a future paper. Also, the transition region emission measure is not evaluated in this paper.

3.1. *Single-fluid Parameter Variations*

In the first set of results we assume the plasma behaves as a single fluid, and ignore heat flux limiting and ionization non-equilibrium. Figure 1 shows temperature (upper panel) and density (lower panel) as a function of time for a single nanoflare in a loop with $2L = 80$ Mm for four different pulse durations, τ: 20, 40, 200, and 500 s. The heating function takes the form of a triangular pulse. The peak heating rate is varied such that the total energy input is 10 ergs cm^{-3} for all cases. These parameters correspond roughly to the bright AR core loops. In order to ensure that the temperature and density do not become negative, a small background heating of magnitude $H_{bg} = 3.5 \times 10^{-5}$ ergs cm^{-3} s^{-1} is enforced at all times. It can be seen that shorter pulses give higher temperatures, as is expected. Furthermore, in this early heating phase, one would expect the maximum temperature to scale roughly as $H_0^{2/7}$ (where H_0 is the peak heating rate); this is approximately what is found. On the other hand, the different pulse durations give approximately the same maximum density, with the shortest pulse reaching its peak value a few hundred seconds before the longest.

The top left panel of Figure 2 shows the corresponding emission measure distributions, EM(T). The temperature and value of the peak emission measure are the same in all cases and the values of T_m and EM(T_m) are consistent with those found in the studies of core loops. While shorter pulses lead to higher initial temperatures, the shape of the emission measure below T_m is independent of the properties of the heating pulse, indicating that this part of the emission measure distribution cannot provide information about the actual nanoflare duration. It is for this reason that we only show EM(T) for $\log T > \log T_M$.
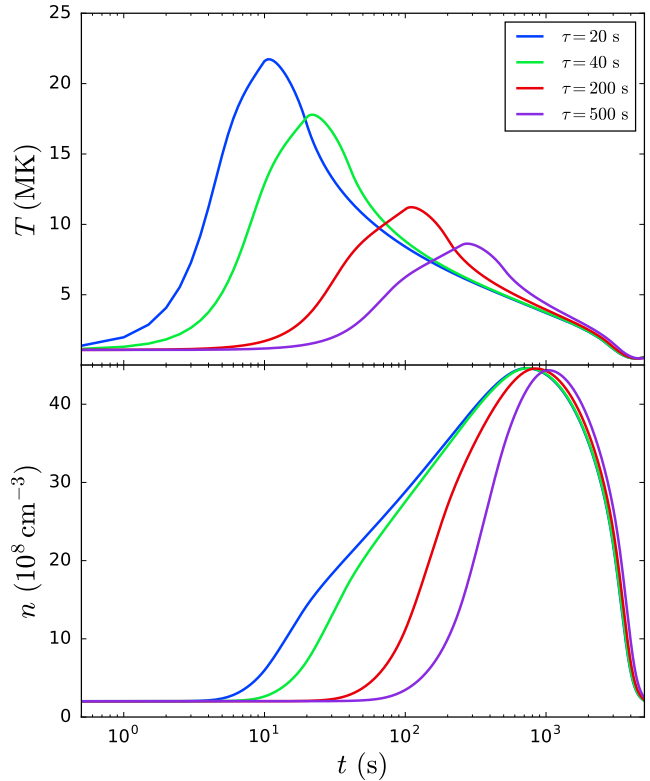

FIG. 1.— Temperature (T) and density (n) profiles for loop full length $2L = 80$ Mm. Each heating profile is triangular in shape with a steady background heating of $h_{bg} = 3.5 \times 10^{-5}$ ergs cm^{-3} s^{-1}. The duration of the heating pulse is varied according to $\tau = 20, 40, 200, 500$ s, with each value of τ indicated by a different color. The total energy injected into the loop is fixed at $q = 10$ ergs cm^{-3}. Note that time is shown on a log scale to emphasize the behavior of the heating phase.

All cases show evidence of the heating phase, namely the bump on EM(T) at $\log(T) = 6.85, 7, 7.2$ and 7.3, and is most obvious for the longer pulses.

Below these bumps the emission measure scales as $T^{-5} - T^{-5.5}$ to close to T_m for all cases, again indicating that information about the heating process is lost, even at these temperatures. However, detection of such emission above T_m would still be evidence for nanoflare heating, though of undetermined duration. For integration over the lifetime of unresolved structures lying transverse to the line of sight, one can write down an expression EM(T) $\sim n^2\tau_{cool}(n,T)$ which simply states that what matters for determining EM(T) is how long the plasma spends at any given temperature (e.g. Cargill 1994; Cargill & Klimchuk 2004). For an analytic solution for the cooling, one can formally define $\tau_{cool}(n,T) = (T/(dT/dt))$. In the absence of a formal solution, order of magnitude scalings can be used: the difference with analytic solutions being a numerical factor. To obtain an expression EM(T) $\propto T^{-b}$, one needs to provide a relation between T and n. For conductive cooling of the corona, one can write $\tau_{cool} \sim nL^2T^{-5/2}$, giving EM $\sim n^3L^2T^{-5/2}$. In determining the relationship between T and n, two limits are those of constant density and constant pressure. The former gives static conductive cooling (e.g. Antiochos & Sturrock 1976) and the latter evaporative cooling with constant thermal energy
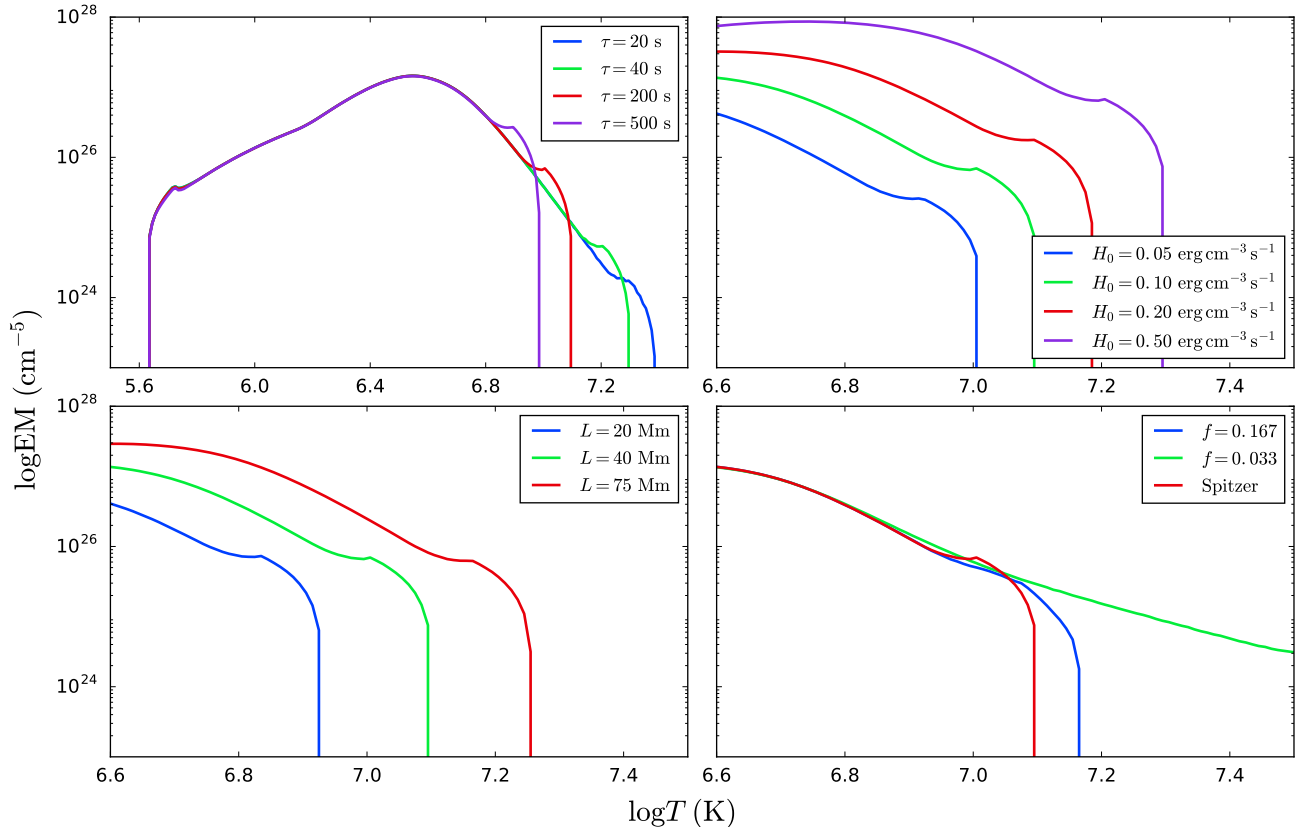
FIG. 2.— EM(T) for a nanoflare in an AR loop. The four panels show the variations in τ (the nanoflare duration), H_0 (the peak heating rate), L (the coronal loop half length), and the heat flux model. The baseline parameters are $\tau = 200$ s, $H_0 = 0.1$ ergs cm^{-3} s^{-1}, $2L = 80$ Mm. The relevant parameters and associated colors are shown in each panel. EM(T) is calculated according to the procedure outlined in the beginning of Section 3.

(e.g. Antiochos & Sturrock 1978), which then lead to $b = 5/2$ and $11/2$ respectively. Our results in the top left panel of Figure 2 are consistent with the latter.

The top right and bottom left panels of Figure 2 show the effect of varying the peak heating rate H_0 (with fixed τ such that the total energy injected increases) and loop length L. In all cases the pulse length is 200 s. The signature of nanoflare heating around and above 10 MK persists. When the heating amplitude increases, the value of T_m increases above the values seen in AR cores, suggesting an upper limit on the nanoflare energy (and hence on the time between nanoflares; see Cargill 2014). Increasing the length also retains the signatures of the hot component, while the gravitational coronal stratification plays no role at these temperatures. Since the aspect ratio remains fixed, the emission measure will increase with length. It is also important to note that changing the background density by an order of magnitude (not shown) retains the hot component. This suggests that even in the intermediate frequency nanoflare regime there should be signatures above T_m and will be discussed further in Paper II

3.2. Heat Flux Limiter

The bottom right panel of Figure 2 shows the effect of using a flux limiter versus Spitzer conduction on the emission measure distribution. Two values of f, 1/6 (blue line) and 1/30 (green line) are shown.

As expected, inclusion of a limiter extends EM(T) to higher temperatures, though this is only notable above 10 MK. As the temperature falls to this value, evaporative upflows have increased the coronal density so that the Spitzer description is recovered. Above 10 MK flux limiting gradually becomes important, albeit with a small emission measure. For this case $\tau_{cool} \sim LT^{-1/2}$ so that the parameter b lies between 1/2 and 5/2, depending on the assumption about n. For $f = 1/30$, $b = 5/2$ is found in the bottom right panel of Figure 2. Since the free streaming limit slows conduction cooling relative to that given by Spitzer, the plasma will spend more time at any given temperature, leading to smaller values of b. Similar conclusions hold for other conduction models (e.g. the non-local model discussed in the coronal context by Karpen & DeVore 1987; West et al. 2008) since they all inhibit conduction. While limiting of conduction is often regarded as an important process in coronal cooling, these results suggest that for nanoflare heating it may not be that important.

3.3. Two-fluid Effects

We now consider the role of two-fluid effects, focusing on cases when only the electrons or ions are heated in order to highlight the essential difference between the two scenarios. Intermediate cases of energy distribution will be considered elsewhere. Figure 3 shows the temperature (top row) and density (bottom row) as a function of time for $\tau = 20, 500$ s (blue and purple lines, respectively). Electron (ion) heating is shown in the left (right)
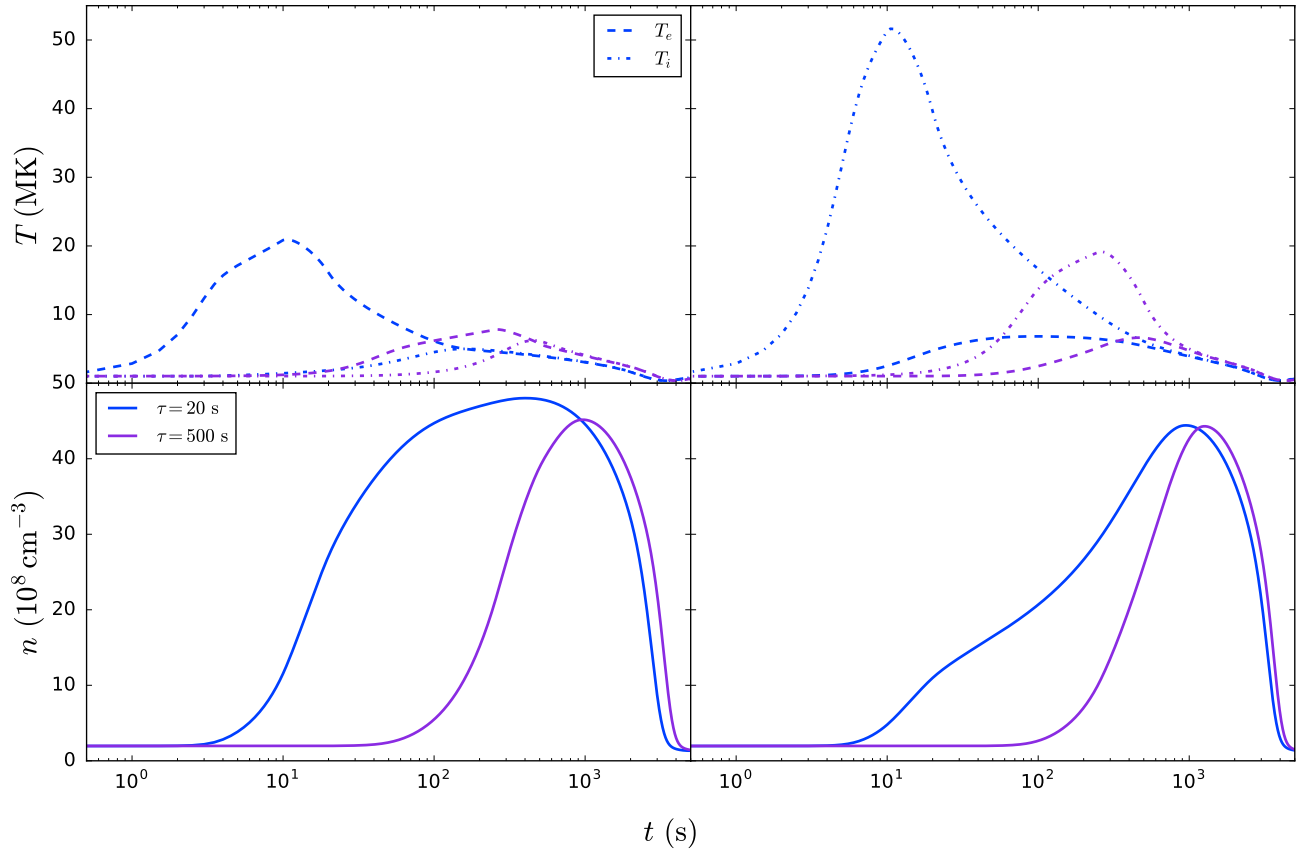
FIG. 3.— Temperature (top row) and density (bottom row) for the cases of electron heating (left column) and ion heating (right column). In each panel, two different heating durations, $\tau = 20$ s and $\tau = 500$ s, are shown with the blue and purple lines, respectively. Electron (ion) temperatures are represented by dashed (dot-dashed) lines.

column and the solid (dashed) lines show the electron (ion) temperature. For electron heating, a comparison with Figure 1 shows the expected similar peak electron temperature from the balance between heating and electron thermal conduction. Ion heating leads to significantly higher temperatures due to the relative weakness of ion thermal conduction, consistent with the expected enhancement of $(\kappa_{0,e}/\kappa_{0,i})^{2/7}$. Cooling occurs by a combination of electron and ion thermal conduction and temperature equilibration. For electron heating, equilibration occurs at 150 (450) s for short (long) pulses whereas for ion heating, these become 1000 (1500) s

The reason for slower equilibration for ion heating can be found in the density plots. These show that while the peak values of the density are similar for both heating mechanisms, the temporal behvior diffors for ion heating with shorts pulses: for these cases, the density takes considerably longer to reach the maximum value. This can be attributed to the relative weakness of ion thermal conduction. Examination of Equation A18 and Equation A23 shows that an upward enthalpy flux can only be effective for ion heating once temperature equilibration has become significant and an electron heat flux established. In turn, once the upflow begins, the coronal density increases, making equilibration more effective. Thus, once temperature equilibration starts to be effective, these processes combine to give a rapid increase in density, as shown.

The black curves in Figure 4 show the resulting $\mathrm{EM}(T)$ for $\tau = 20$ s (left panel) and $\tau = 500$ s (right panel). In the case of electron heating and $\tau = 20$ s, the emission measure slope differs significantly from that of the single-fluid case. For $6.6 < \log T < 6.8$, $\mathrm{EM}(T)$ is considerably steeper compared to the single-fluid case; for $\log T > 6.8$, $\mathrm{EM}(T)$ becomes comparably more shallow. Recall that in the case of pure conductive cooling, $b = 11/2$; however, this requires constant pressure p such that $n \propto T^{-1}$ (see Subsection 3.1). Figure 5 shows pressure and density as a function of temperature for the short pulse ($\tau = 20$ s) case; both the single-fluid case and the case where only the electrons are heated are shown. Here, note that while $p_e + p_i$, the total pressure, is constant during the early heating phase (i.e. $\log T > 6.8$), the electron pressure, p_e is not. Thus, $n \propto T_e^{-1}$ does not hold for the two-fluid case. Comparing the two density curves in Figure 5 yields $n \propto T^{-\delta}$, where $\delta < 1$, and consequently a more shallow emission measure slope b', with $b' < 11/2$.

An important caveat to this result is that this more shallow slope is unlikely to be observed because of non-equilibrium ionization (see Subsection 3.4). Additionally, it may be an artifact of the 0D nature of the EBTEL model as more advanced loop models (see Figure 8 and the accompanying discussion) show a much lower and constant density during this early heating and cooling phase as some finite amount of time is required to get the material moving up the loop. For constant density, $\delta \to 0$ and $b \to 5/2$, suggesting that more realistic emission measure models of impulsive heating would yield flatter, but significantly weaker emission for $\log T > 6.8$. NOTE: Have not addressed the steepened EM slope between 6.6 and 6.8. Is this significant? Appendix figure showing delta_pe terms seems to suggest that equilibration plays a role in this temperature range.

In the case where the heating pulse duration is long, $\tau = 500$ s, the difference between the two-fluid and single-fluid emission measure distributions is diminished. Because the electrons are heated slowly, they do not have much time to evolve out of equilibrium with the ions. This in turn heavily dampens the Coulomb exchange term. Additionally, in the case where only the ions are heated, for both $\tau = 20$ s and $\tau = 500$ s, $\mathrm{EM}(T)$ is truncated sharply near $\log T \sim 6.9$. Becuase $\mathrm{EM}(T)$ is constructed from the electron temperature, the emission measure never sees $\log T \geq 7$ because the Coulomb coupling timescale, during the early heating phase where $T_i \gg T_e$ and the density is low, is much larger than the ion thermal conduction timescale. Thus, by the time the electrons can "see" the ions, they have cooled far below their peak temperature.

3.4. *Ionization Non-equilibrium*

The final set of results includes our approximate treatment of non-equilibrium ionization. The red curves in the left (right) panel of Figure 6 show T_{eff} for $\tau = 20\,(500)$ s for the single-fluid, electron heating, and ion heating cases. For comparison, equivalent results for T (single fluid) and T_e (two fluid) that assume ionization equilibrium are shown in black. For all cases, T_{eff} never rises above 10 MK for the short pulse and 8 MK for the long pulse. Thus, for the short pulse, because a sufficiently long time is required to ionize the plasma, the hottest electron temperatures are never likely to be detectable. For the longer pulse, the slow heating gives the ionization states the opportunity to "catch up"; thus T_{eff} is a reasonable reflection of the actual plasma state.

The red curves in Figure 4 show the corresponding $\mathrm{EM}(T_{eff})$. The effect of ionization non-equilibrium is to truncate EM around or below 10 MK. The bump on the distribution characteristic of the heating phase is also relocated to lower temperatures. This confirms the earlier comment that, at least for short pulses, the hot electron plasma above 10 MK is undetectable. While the heating signature is shifted to smaller values of T_{eff}, one has no way of knowing the duration of the pulse that generates it. Thus it seems as if the temperature range $T_m < T < 10$ MK is the optimal one for searching for this hot component as well as direct signatures of the heating. However, it is difficult to "map" what would be seen in such a state of ionization non-equilibrium back to the real system.

4. DISCUSSION

In this paper we have looked at the hot plasma component that arises from a single nanoflare. When ionization equilibrium is assumed, it is shown that this component is ubiquitous and has a distribution of emission measure as a function of temperature consistent with conductive cooling for either Spitzer or free-streaming conduction models. There is a characteristic "bump" on the emission measure at or above 10 MK that is a direct manifestation of the heating process. While both these results suggest quantitative ways of measuring this plasma in the future, any significant lack of ionization equilibrium leads to a failure to be actually able to observe this hot plasma in most cases.

From the single nanoflare results for a single fluid, it appears that it is not possible to say anything about the
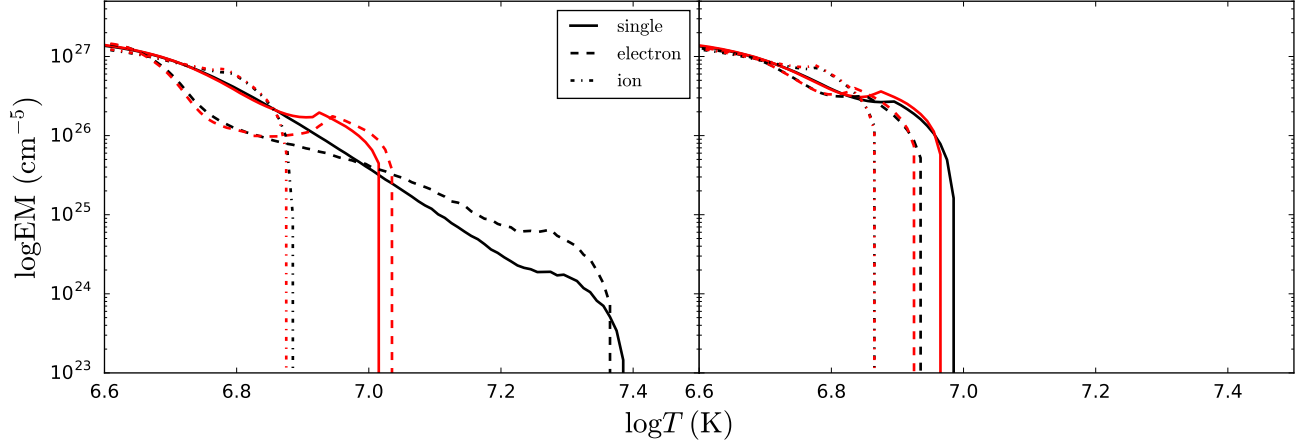
FIG. 4.— EM(T) (black) and EM(T_{eff}) (red) for pulse durations of 20 s (left panel) and 500 s (right panel) for the single-fluid (solid), electron heating (dashed), and ion heating (dot-dashed) cases.
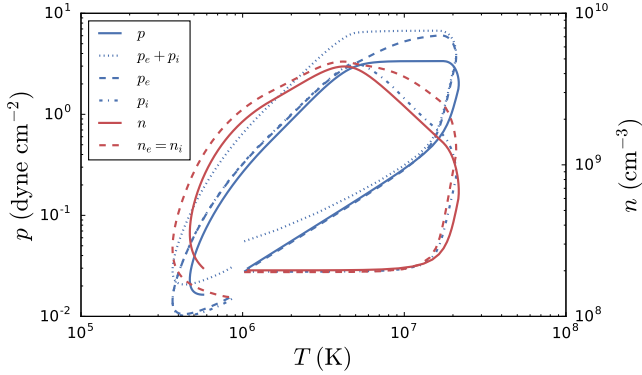

FIG. 5.— Pressure (blue lines) and density (red lines) as a function of temperature for the short pulse case ($\tau = 20$ s). Single-fluid (solid) and electron heating (dashed) cases are shown. The total pressure in the two-fluid case, $p_e + p_i$, is denoted by the dotted blue line. Note that the total pressure in both the single-fluid and electron heating cases is constant between about 4 MK and 20 MK.

plasma in excess of 10 MK. If the electrons are heated, this plasma exists, with electron temperature in excess of 10 MK, but nothing can be said about it. It is effectively a "dark" hot plasma. The case of proton heating is even more complicated. On the other hand, the bump on EM(T) associated with the heating does seem to be shifted down in temperature.

Current instrumentation does not allow for a determination of the partition of energy between electron and ion populations by the as yet undetermined coronal heating mechanism based on EM(T) alone. For $T < T_M$, the

density is sufficiently high such that $\tau_{ei} \to 0$ and the two populations are always in equilibrium; any information about which species was preferentially heated has been lost. In order to discriminate between the heating of one species over another, greater constraints must be placed on EM(T) for $T > T_M$. Here, for example, a steep drop after T_M and an extended tail near 10^7 K is a possible signature of electron heating while a sharp cutoff before 10^7 K could be a signature of ion heating. As seen in Figure 4, these signatures are exaggerated the more impulsive the heating and ionization non-equilibrium does not preclude a determination of the energy partition.

A full discussion of where this leads for present and future measurements will be deferred to Paper II where we discuss results for nanoflare trains, including the important "intermediate frequency" nanoflare case. But one can conclude (i) present day observations do not seem capable of making quantitative statements about the "hot" component, though they are highly suggestive of its existence and (ii) future measurements should be concentrated in the temperature regime $10^{6.6}$ – 10^7 K rather than at higher temperatures. The MaGIXS instrument, due to fly in 2017, is well positioned to do this. Finally, the rocket results of Caspi et al. (2015) pose a problem in that if only quiescent coronal plasma were being observed, it is difficult to understand how an emission measure distribution characteristic of Spitzer conduction can arise. It seems possible that a microflare or small flare occurred during the observations.

APPENDIX

The two-fluid field-aligned hydrodynamic mass and energy equations, as given by Bradshaw & Cargill (2013), are

$$\frac{\partial \rho}{\partial t} = -\frac{\partial(\rho v)}{\partial s} \tag{A1}$$

$$\frac{\partial E_e}{\partial t} + \frac{\partial}{\partial s}[(E_e + p_e)v] = v\frac{\partial p_e}{\partial s} - \frac{\partial F_{ce}}{\partial s} + \frac{1}{\gamma - 1}k_B n \nu_{ei}(T_i - T_e) - n^2 \Lambda(T_e) + Q_e, \tag{A2}$$

$$\frac{\partial E_i}{\partial t} + \frac{\partial}{\partial s}[(E_i + p_i)v] = -v\frac{\partial p_e}{\partial s} - \frac{\partial F_{ci}}{\partial s} + \frac{1}{\gamma - 1}k_B n \nu_{ei}(T_e - T_i) + \frac{\partial}{\partial s}\left(\frac{4}{3}\mu_i v \frac{\partial v}{\partial s}\right) + \rho v g_\parallel + Q_i, \tag{A3}$$
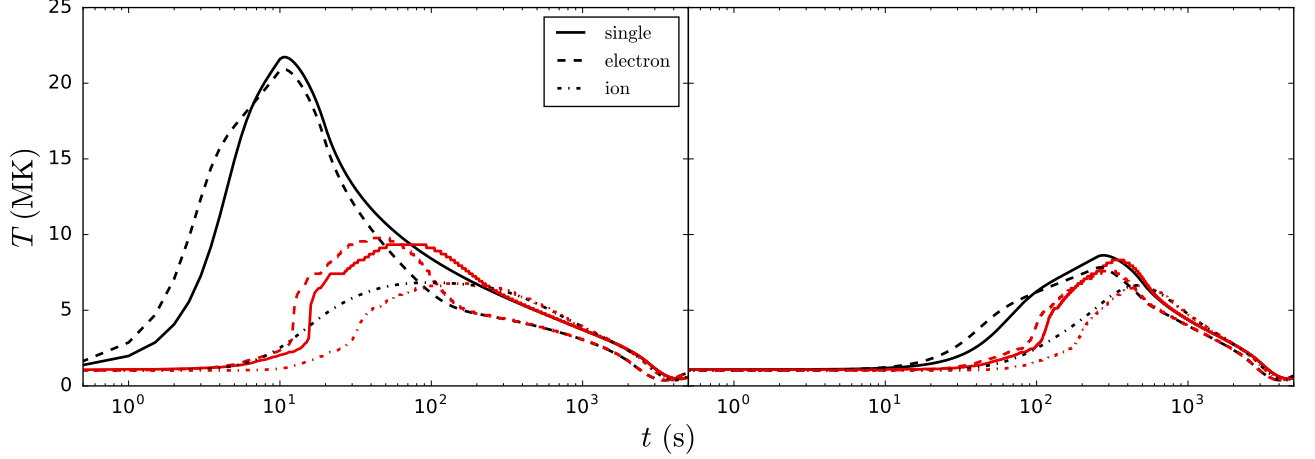
FIG. 6.— T (black) and T_{eff} (red) for pulse durations of 20 s (left panel) and 500 s (right panel). T and T_{eff} are shown for the single-fluid case (solid) as well as the cases where only the electrons (dashed) or only the ions (dot-dashed) are heated.

where

$$E_e = \frac{p_e}{\gamma - 1}, \tag{A4}$$

$$E_i = \frac{p_i}{\gamma - 1} + \frac{\rho v^2}{2}, \tag{A5}$$

and we assume closure through the ideal gas law, $p_e = k_B n T_e$, $p_i = k_B n T_i$. Note that we have assumed quasi-neutrality such that $n_e = n_i = n$ and $v_e = v_i = v$. It then follows that $\rho = m_e n_e + m_i n_i \approx m_i n$.

Note the right-hand side of Equation A2 and Equation A3: the first term represents the energy loss or gain as the fluids move through the electric field that maintains quasi-neutrality, given by $E = -(1/n)\partial p_e/\partial s$; the third term models the exhange of energy between the electron and ion populations via binary Coulomb collisions and is attributed to Braginskii (1965). Though the expression presented here differs by a factor of 2 compared to that of Braginskii, we maintain that the electron-ion equilibration time is not significantly changed by this relatively small numerical factor.

Plugging in these expressions for E_e and E_i and using the assumptions of sub-sonic flows ($v < C_s$) and loops shorter than a gravitational scale height ($L < 150$ Mm) as outlined in Klimchuk et al. (2008), the two-fluid field-aligned hydrodynamic energy equations can be written,

$$\frac{1}{\gamma - 1}\frac{\partial p_e}{\partial t} + \frac{\gamma}{\gamma - 1}\frac{\partial}{\partial s}(p_e v) = v\frac{\partial p_e}{\partial s} - \frac{\partial F_{ce}}{\partial s} + \frac{1}{\gamma - 1}k_B n \nu_{ei}(T_i - T_e) - n^2\Lambda(T_e) + Q_e, \tag{A6}$$

$$\frac{1}{\gamma - 1}\frac{\partial p_i}{\partial t} + \frac{\gamma}{\gamma - 1}\frac{\partial}{\partial s}(p_i v) = -v\frac{\partial p_e}{\partial s} - \frac{\partial F_{ci}}{\partial s} + \frac{1}{\gamma - 1}k_B n \nu_{ei}(T_e - T_i) + Q_i. \tag{A7}$$

Notice that we have dropped the ion viscous and gravitational terms from Equation A3 as well as the kinetic energy term from Equation A5. Q_e and Q_i represent the electron and ion heating terms, respectively. F_{ce} and F_{ci} are the electron and ion heat flux terms, respectively. In the case of Spitzer conduction, $\kappa_{0,e} = 7.8 \times 10^{-7}$ and $\kappa_{0,i} = 3.2 \times 10^{-8}$.

The analysis now follows that of Klimchuk et al. (2008) and Cargill et al. (2012a). Assuming symmetry about the loop apex, we integrate Equation A6 and Equation A7 over the coronal loop half-length L,

$$\frac{L}{\gamma - 1}\frac{d\bar{p}_e}{dt} = \frac{\gamma}{\gamma - 1}(p_e v)_0 + F_{ce,0} + \psi_C - \mathcal{R}_C + L\bar{Q}_e, \tag{A8}$$

$$\frac{L}{\gamma - 1}\frac{d\bar{p}_i}{dt} = \frac{\gamma}{\gamma - 1}(p_i v)_0 + F_{ci,0} - \psi_C + L\bar{Q}_i, \tag{A9}$$

where we have assumed the enthalpy flux and heat flux go to zero at the loop apex, $R_C = \int_C \mathrm{d}s\, n^2\Lambda(T_e)$ and,

$$\psi_C = \int_C \mathrm{d}s\, v\frac{\partial p_e}{\partial s} + \int_C \mathrm{d}s\, \frac{k_B}{\gamma - 1}n \nu_{ei}(T_i - T_e). \tag{A10}$$

Similarly, integrating over the TR portion of the loop of thickness ℓ, we obtain,

$$\frac{\gamma}{\gamma-1}(p_e v)_0 = -F_{ce,0} + \psi_{TR} - \mathcal{R}_{TR}, \tag{A11}$$

$$\frac{\gamma}{\gamma-1}(p_i v)_0 = -F_{ci,0} - \psi_{TR}, \tag{A12}$$

where several terms are neglected because $\ell \ll L$ (Klimchuk et al. 2008). Additionally, we have assumed that the enthalpy flux and heat flux go to zero at the top of the chromosphere, $R_{TR} = \int_{TR} \mathrm{d}s\, n^2 \Lambda(T_e)$ and

$$\psi_{TR} = \int_{TR} \mathrm{d}s\, v \frac{\partial p_e}{\partial s} + \int_{TR} \mathrm{d}s\, \frac{k_B}{\gamma-1} n \nu_{ei}(T_i - T_e). \tag{A13}$$

The second term in this expression is usually small, but is retained for completeness. Plugging Equation A11 (Equation A12) into Equation A8 (Equation A9),

$$\frac{L}{\gamma-1}\frac{d\bar{p}_e}{dt} = \psi_{TR} + \psi_C - (\mathcal{R}_C + \mathcal{R}_{TR}) + L\bar{Q}_e, \tag{A14}$$

$$\frac{L}{\gamma-1}\frac{d\bar{p}_i}{dt} = -(\psi_C + \psi_{TR}) + L\bar{Q}_i. \tag{A15}$$

Note that adding Equation A14 and Equation A15 gives the correct single-fluid EBTEL model (i.e. Equation 2).

As in the single-fluid case, we find that the spatially-integrated coronal density evolution is described by,

$$L\frac{d\bar{n}}{dt} = (nv)_0. \tag{A16}$$

Using Equation A11 and the equation of state for p_e, the above equation can be written as

$$(nv)_0 = \frac{(p_e v)_0}{k_B T_{e,0}} = \frac{c_2(\gamma-1)}{c_3 \gamma k_B \bar{T}_e}(-F_{ce,0} - \mathcal{R}_{TR} + \psi_{TR}), \tag{A17}$$

$$L\frac{d\bar{n}}{dt} = \frac{c_2(\gamma-1)}{c_3 \gamma k_B \bar{T}_e}(-F_{ce,0} - \mathcal{R}_{TR} + \psi_{TR}). \tag{A18}$$

To obtain Equation 7, Equation 8, and Equation 9, we need to find expressions for ψ_C and ψ_{TR}. Recall that ψ_C and ψ_{TR} are comprised of terms associated with the quasi-neutral electric field and temperature equilibration. The integral of the former can be considered as the gain or loss of energy associated with plasma motion through the net electric potential. Consider the first integral in the definition of ψ_C. Using integration by parts,

$$\int_C \mathrm{d}s\, v \frac{\partial p_e}{\partial s} = (p_e v)\Big|_{\text{``0''}}^{\text{``a''}} - \int_C \mathrm{d}v\, p_e = -(p_e v)_0 - \int_C \mathrm{d}v\, p_e \approx -(p_e v)_0 - \bar{p}_e \int_C \mathrm{d}v = -(p_e v)_0 + \bar{p}_e v_0 \approx 0. \tag{A19}$$

Thus, we can express ψ_C as

$$\psi_C \approx \frac{k_B L}{\gamma-1} \bar{n} \nu_{ei}(\bar{T}_i - \bar{T}_e), \tag{A20}$$

where $\nu_{ei} = \nu_{ei}(\bar{T}_e, \bar{n})$. To find an expression for ψ_{TR}, we first note that, using the equation of state for both the electrons and the ions and the quasi-neutrality condition $(n_e = n_i)$,

$$\frac{p_e v}{p_i v} = \frac{T_e}{T_i}. \tag{A21}$$

Evaluating this expression at the TR-corona interface (denoted by "0"), plugging in Equation A11 and Equation A12,

$$\frac{-F_{ce,0} + \psi_{TR} - \mathcal{R}_{TR}}{-F_{ci,0} - \psi_{TR}} = \xi, \tag{A22}$$

where $\xi \equiv T_{e,0}/T_{i,0}$. Solving for ψ_{TR}, we find,

$$\psi_{TR} = \frac{1}{1+\xi}(F_{ce,0} + \mathcal{R}_{TR} - \xi F_{ci,0}). \tag{A23}$$

Plugging Equation A20 and Equation A23 into Equation A14, Equation A15, and Equation A18 gives us our set of two-fluid EBTEL equations as given in Equation 7, Equation 8, and Equation 9. The same prescription for c_1, c_2, and c_3 as in the single-fluid version of EBTEL. As discussed in Cargill et al. (2012a), these play little role in the early heating phase when two-fluid effects are important.
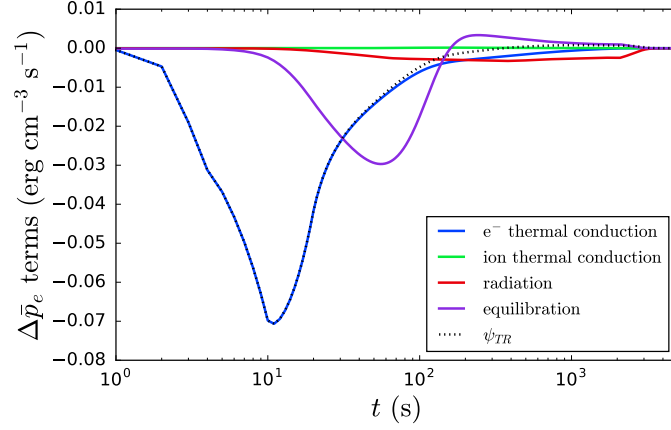
FIG. 7.— Contributions to the EBTEL two-fluid electron energy evolution by thermal conduction, radiation, and binary Coulomb interactions. The parameters for the loop evolution are the same as those for the electron heating, $\tau = 20$ s case discussed in Section 3. The exact expressions for each curve are found in Equation A24. The black dotted line shows ψ_{TR} to emphasize its importance in the derivation of the two-fluid equations.
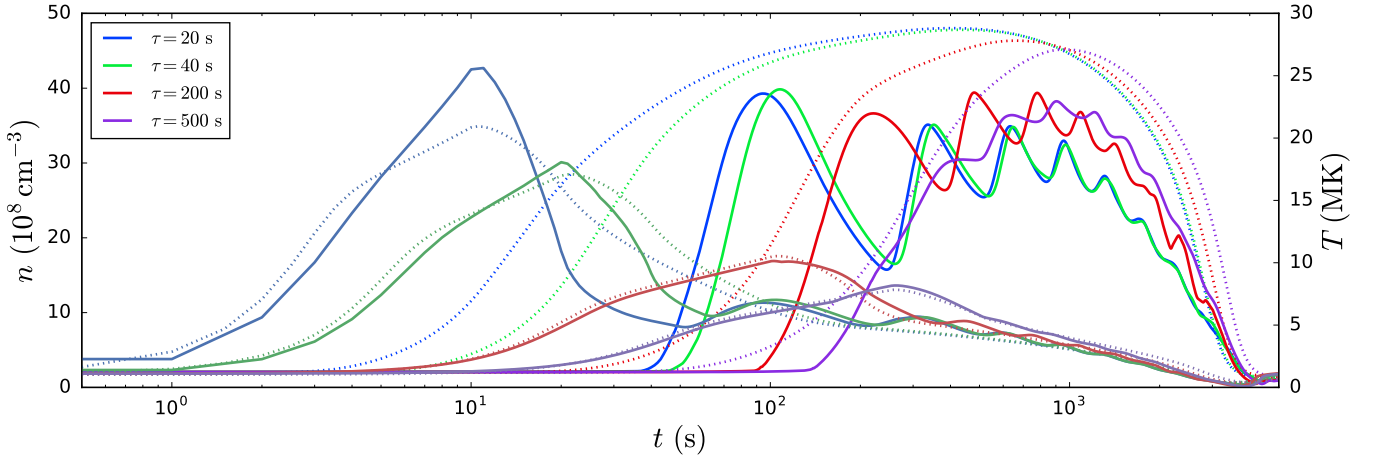

FIG. 8.— Comparison between HYDRAD (solid lines) and EBTEL (dotted lines) results for varying pulse duration, τ. The associated colors for each value of τ are shown in the legend. Density is on the left axis and temperature on the right, with the temperature curves represented by the more muted color palette. The parameters are equivalent to the base parameter set for varying τ given in Section 3.

Plugging Equation A23 into Equation 7, the electron energy evolution equation can be written,

$$\frac{1}{\gamma - 1}\frac{d\bar{p}_e}{dt} = \frac{1}{L(1+\xi)}F_{ce,0} - \frac{\xi}{L(1+\xi)}F_{ci,0} - \frac{\xi(c_1+1)+1}{L(1+\xi)}\mathcal{R}_C + \frac{k_B}{\gamma-1}\bar{n}\nu_{ei}(\bar{T}_i - \bar{T}_e) + \bar{Q}_e, \qquad \text{(A24)}$$

where the first two terms on the right-hand side represent the contributions from electron and ion thermal conduction, the third term represents losses from radiation, and the last two terms are as before. Figure 7 shows the contribution of each term, with the exception of the heating term, $\bar{Q}_e$. As expected, (electron) thermal conduction dominates during the early heating and cooling phase and losses from radiation takeover in the late draining and cooling stage. Between these two phases, energy exchange between the two species is important to the evolution of the electron energy. ψ_{TR}, indicated by the black dotted line, is included to show its importance in the formation of the two-fluid EBTEL equations.

To validate our new two-fluid EBTEL model, we compare our results for varying τ and electron heating (as discussed in Section 3) against the 1D field-aligned hydrodynamic loop model HYDRAD (Bradshaw & Cargill 2013). Figure 8 shows density (left axis, bright color palette) and temperature (right axis, muted color palette) as functions of time for equivalent two-fluid EBTEL (dotted lines) and HYDRAD (solid lines) runs. In order to compare HYDRAD against a 0D model, we have averaged the electron temperature and density over the top 50% of the loop. In the two-fluid EBTEL runs, the background heating has been adjusted to ensure that EBTEL and HYDRAD have the same initial density.

For $\tau \geq 200$ s there is excellent agreement in T_e between the HYDRAD and two-fluid EBTEL results; for $\tau = 20, 40$ s, there is generally good agreement with some discrepancies in between the time at which the temperature peaks and the time at which radiation becomes the dominant cooling mechanism. The most glaring difference lies in the density evolution for $\tau < 200$ s. Here, the two-fluid EBTEL density begins to rise almost immediately following the onset of

heating. As a result, the emission measure calculated from the two-fluid EBTEL model "sees" temperatures well in excess of 10 MK. In the HYDRAD loop model, this will not be the case: there will be a delay in the upflow of material because some finite amount of time is required to get material moving up the loop, an effect inherently absent from 0D models. The more gentle the heating profile is, the less severe this discrepancy will be since the rise in the two-fluid EBTEL density will be more delayed and the loop will be cooler.

REFERENCES

Antiochos, S. K., & Sturrock, P. A. 1976, Sol. Phys., 49, 359
—. 1978, ApJ, 220, 1137
Barnes, W. T., Cargill, P. J., & Bradshaw, S. J. 2016, in preparation
Bradshaw, S. J. 2009, A&A, 502, 409
Bradshaw, S. J., & Cargill, P. J. 2006, A&A, 458, 987
—. 2010a, ApJ, 717, 163
—. 2010b, ApJ, 710, L39
—. 2013, ApJ, 770, 12
Bradshaw, S. J., Klimchuk, J. A., & Reep, J. W. 2012, ApJ, 758, 53
Braginskii, S. I. 1965, Reviews of Plasma Physics, 1, 205
Brosius, J. W., Daw, A. N., & Rabin, D. M. 2014, ApJ, 790, 112
Cargill, P. J. 1994, ApJ, 422, 381
Cargill, P. J. 1995, in Proceedings of the 15th National Solar Observatory/Sacramento Peak Summer Workshop (Sunspot, New Mexico, USA: World Scientific), 17
—. 2014, ApJ, 784, 49
Cargill, P. J., Bradshaw, S. J., & Klimchuk, J. A. 2012a, ApJ, 752, 161
—. 2012b, ApJ, 758, 5
Cargill, P. J., & Klimchuk, J. A. 2004, ApJ, 605, 911
Cargill, P. J., Warren, H. P., & Bradshaw, S. J. 2015, Phil. Trans. R. Soc. A, 373, 20140260
Caspi, A., Woods, T. N., & Warren, H. P. 2015, ApJ, 802, L2
Ciaravella, A., Peres, G., & Serio, S. 1991, Sol. Phys., 132, 279
Culhane, J. L., Harra, L. K., James, A. M., et al. 2007, Sol. Phys., 243, 19
De Moortel, I., & Browning, P. 2015, Philosophical Transactions of the Royal Society of London Series A, 373, 40269
Del Zanna, G., & Mason, H. E. 2014, A&A, 565, A14
Del Zanna, G., Tripathi, D., Mason, H., Subramanian, S., & O'Dwyer, B. 2015, A&A, 573, A104
Drake, J. F., & Swisdak, M. 2014, Physics of Plasmas (1994-present), 21, 072903
Gburek, S., Sylwester, J., Kowalinski, M., et al. 2011, Solar System Research, 45, 189
Golub, L., Deluca, E., Austin, G., et al. 2007, Sol. Phys., 243, 63
Ishikawa, S.-n., Glesener, L., Christe, S., et al. 2014, Publications of the Astronomical Society of Japan, 66, S15
Karpen, J. T., & DeVore, C. R. 1987, ApJ, 320, 904
Klimchuk, J. A., Patsourakos, S., & Cargill, P. J. 2008, ApJ, 682, 1351
Kosugi, T., Matsuzaki, K., Sakao, T., et al. 2007, Sol. Phys., 243, 3

Krucker, S., Christe, S., Glesener, L., et al. 2011, in Society of Photo-Optical Instrumentation Engineers (SPIE) Conference Series, Vol. 8147, 814705
Lemen, J. R., Title, A. M., Akin, D. J., et al. 2012, Sol. Phys., 275, 17
Ljepojevic, N. N., & MacNeice, P. 1989, Physical Review A, 40, 981
Markovskii, S. A., & Hollweg, J. V. 2004, ApJ, 609, 1112
Miceli, M., Reale, F., Gburek, S., et al. 2012, A&A, 544, A139
Ofman, L., Klimchuk, J. A., & Davila, J. M. 1998, ApJ, 493, 474
Ono, Y., Yamada, M., Akao, T., Tajima, T., & Matsumoto, R. 1996, Phys. Rev. Lett., 76, 3328
Parker, E. N. 1988, ApJ, 330, 474
Pesnell, W. D., Thompson, B. J., & Chamberlin, P. C. 2012, Sol. Phys., 275, 3
Petralia, A., Reale, F., Testa, P., & Del Zanna, G. 2014, A&A, 564, A3
Reale, F., Guarrasi, M., Testa, P., et al. 2011, ApJ, 736, L16
Reale, F., & Orlando, S. 2008, ApJ, 684, 715
Reale, F., Testa, P., Klimchuk, J. A., & Parenti, S. 2009, ApJ, 698, 756
Reep, J. W., Bradshaw, S. J., & Klimchuk, J. A. 2013, ApJ, 764, 193
Schmelz, J. T., & Pathak, S. 2012, ApJ, 756, 126
Schmelz, J. T., Saar, S. H., DeLuca, E. E., et al. 2009, ApJ, 693, L131
Spitzer, L., & Härm, R. 1953, Physical Review, 89, 977
Sylwester, J., Kuzin, S., Kotov, Y. D., Farnik, F., & Reale, F. 2008, Journal of Astrophysics and Astronomy, 29, 339
Tajfirouze, E., Reale, F., Petralia, A., & Testa, P. 2016, ApJ, 816, 12
Testa, P., & Reale, F. 2012, ApJ, 750, L10
Testa, P., Reale, F., Landi, E., DeLuca, E. E., & Kashyap, V. 2011, ApJ, 728, 30
Tripathi, D., Klimchuk, J. A., & Mason, H. E. 2011, ApJ, 740, 111
Warren, H. P., Brooks, D. H., & Winebarger, A. R. 2011, ApJ, 734, 90
Warren, H. P., Winebarger, A. R., & Brooks, D. H. 2012, ApJ, 759, 141
West, M. J., Bradshaw, S. J., & Cargill, P. J. 2008, Sol. Phys., 252, 89
Winebarger, A. R., Schmelz, J. T., Warren, H. P., Saar, S. H., & Kashyap, V. L. 2011, ApJ, 740, 2
Winebarger, A. R., Warren, H. P., Schmelz, J. T., et al. 2012, ApJ, 746, L17